PJHRD
Philippine Journal of Health Research and Development
University of the Philippines Manila - The Health Sciences Center
Information, Publication and public affairs Office (IPPAO)
8/F Philippine General Hospital Complex, Taft Avenue, Manila 1000 Philippines
Online ISSN: 2783-042X
April-June
VOL. 28 NO. 2 2024
PAGE 56-66

ORIGINAL ARTICLE

# Nucleobase-substituted Ponatinib Analogues: Molecular Docking, Short Molecular Dynamics, and Drug-likeness Profiling

Vince Lambert H. Padilla*[1,2] and Glenn V. Alea[2]

[1]Department of Pharmaceutical Chemistry, College of Pharmacy, University of the Philippines Manila, Manila, Philippines
[2]Department of Chemistry, College of Science, De La Salle University, Manila, Philippines

## ABSTRACT

**Objectives:** This study aims to assess the drug-likeness and binding of nucleobase-substituted ponatinib analogues towards wild-type and T315I mutant BCR-ABL tyrosine kinases.
**Methodology:** A total of 415 ponatinib analogues, encompassing single and combinatorial modifications on five parts of the drug were generated, profiled in SwissADME, and subjected to molecular docking using AutoDock4. Complexes formed by the top analogues then underwent a 100-ns molecular dynamics simulation with GROMACS.
**Results:** Analogues featuring the replacement of the imidazo[1,2*b*]pyridazine with adenine and cytosine exhibited promising binding free energies, attributed to the presence of primary amines that facilitate crucial hydrogen bond interactions in the hinge region. RMSD, RMSF, and atomic distance analyses of the MD trajectories revealed that the six top analogues formed stable complexes in their inactive DFG-out conformations. Changes in the MMPBSA and MMGBSA-calculated free energies were mainly driven by changes in hydrogen bonds. Furthermore, drug-likeness predictions supported the formulation of most analogues for oral administration.
**Conclusion:** Among the top analogues, VP10004 and VP81014 exhibited the most favorable binding free energies and interactions with the target models, while VP10312 was identified as the most feasible candidate for synthesis.

## Introduction

Abelson (ABL) kinase is a cytoplasmic enzyme involved in the phosphorylation of the tyrosine residues of various proteins inside the cell. This tyrosine kinase is made up of an *N*-myristoyl group at the *N*-terminus, followed by a Src homology 3 – Src homology 2 – tyrosine kinase (SH3-SH2-TK) domain cassette and a final exon region that ends in an F-actin binding domain (FABD). Naturally, the *N*-myristoyl group is involved in the autoregulation of its kinase activity, thereby preventing excessive phosphorylation inside the cell. However, in certain individuals, the t(9;22)(q34;q11) reciprocal translocation transfers a significant portion of the ABL gene from the q arm of chromosome 9 to the q arm of chromosome 22. The resulting abnormality, referred to as the Philadelphia (Ph) chromosome, contains a fusion gene that encodes for BCR-ABL tyrosine kinase — a mutant enzyme that contains a breakpoint cluster region (BCR) instead of an *N*-myristoyl group. Without its autoregulating moiety, the uninhibited kinase activity of BCR-ABL fusion protein then leads to the uncontrolled growth of blood cells observed in Chronic Myeloid Leukemia (CML), as well as in some cases of Acute Lymphoblastic Leukemia (ALL) [1,2].

Over the past years, various drugs called tyrosine kinase inhibitors (TKIs) have been discovered. The 1st generation TKI imatinib is a 2-phenyl amino pyrimidine derivative that targets the inactive form of the enzyme [3]. After its release to the market in 2001, it was observed that the 1st generation TKI had little to no effect on patients whose BCR-ABL contain point mutations in the kinase domain [4,5]. This led to the discovery of nilotinib, and its eventual release to the market in 2007 [6]. Nilotinib was found to be effective against most mutants that are resistant to imatinib. However, patients with the T315I mutation still did not respond to this 2nd generation inhibitor [7]. Further studies aimed at addressing this specific mutation led to the discovery of ponatinib — a 3rd generation TKI that is more potent than the first two and is capable of inhibiting mutated BCR-ABL tyrosine kinases including the T315I mutant [8,9]. Ten months after its US FDA approval in December 2012, ponatinib was voluntarily withdrawn from the market by its manufacturer when post-marketing surveillance data showed that the risk for ponatinib-associated arterial occlusive events are much higher than what was observed during the Phase 2 trials. In December 2013, ponatinib was reintroduced to the market with updated warnings and precautions [10,11].

Ponatinib and its two predecessors work by entering the ATP-binding site while the enzyme is in its DFG-out conformation, effectively depriving the kinase of its phosphorylation co-substrate. These TKIs form a stable complex with the inactive form of the enzyme through several attractive noncovalent interactions. Highlighted as yellow in Figure 1 are moieties that form hydrogen bonds (H-bonds) with the amino acid residues of the enzyme. In the case of imatinib, the pyridine interacts with Met318, the aminopyrimidine with Thr315, the amide with Glu286 and Asp381, and the protonated methylpiperazine with Ile360 and His361. Nilotinib forms the same H-bonds except those with residues 360 and 361. Its trifluoromethyl and methylimidazole groups compensated for the loss of two H-bonds, making it an even more potent inhibitor than imatinib. Both TKIs, however, still rely on their H-bond with Thr315 which is why a T315I mutation — where Threonine is replaced by a hydrogen-bond-incapable and bulkier Isoleucine — renders them inactive. On the other hand, ponatinib is a more potent inhibitor even without the said interaction with Thr315. Moreover, it avoids a steric clash with Ile315 since the amino(pyridinyl)pyrimidine is replaced by an imidazo[1,2*b*]pyridazine (ring system A) which is connected to the methylbenzamide (ring B) via an ethynyl linker (L1), hence the retention of its activity against the T315I mutant [8-12]. Its structural analogue, AP24589, exhibits an additional H-bond with the acyl O of Met318 due to the presence of a carboxamide group [13].

On top of unwanted side effects, another obstacle in leukemia chemotherapy is the existence of consecutive and compound point mutations in BCR-ABL. An example of a consecutive point mutation is T315M. This results when T315I is followed by the replacement of Ile315 with methionine. Cell-based assays reveal that no tyrosine kinase inhibitor, not even ponatinib, is effective against the T315M mutant. In the case of compound mutations, point mutations in BCR-ABL were observed in at least 2 different positions. Ponatinib showed little to no significant reduction in potency against non-T315I compound mutants except for Y253H/E255V. However, in T315I-inclusive compound mutants, ponatinib showed significant loss of effect like the other TKIs, with M244V/T315I as an exception [14].

**Corresponding author's email address:**
vhpadilla@up.edu.ph
**Keywords:** ponatinib, tyrosine kinase inhibition, Philadelphia chromosome, AutoDock, GROMACS, MMPBSA, MMGBSA

These challenges call for the discovery of more potent inhibitors against BCR-ABL tyrosine kinases. In this study, we present the calculated affinities nucleobase-substituted ponatinib analogues, assess their potential drug-likeness, and highlight their notable interactions with the ATP-binding domains of both wild-type and T315I BCR-ABL tyrosine kinase.

# Methodology

### 2.1 Preparation of Protein Files

Appropriate .pdb models of the BCR-ABL tyrosine kinases in their DFG-out conformations were downloaded from the RCSB Protein Data Bank (PDB) (https://www.rcsb.org/). Chain A of PDB ID 3CS9 [15] was isolated and further processed in AutoDockTools (ADT) 1.5.7 [16]. Water molecules and the co-crystallized ligand were deleted, followed by the addition of polar hydrogens. It was noted at this point that the acidic groups of Glu and Asp residues remained as carboxylates while the basic groups of Lys, Arg, and His were in their +1 protonated forms. After adding Kollman charges, it was saved as a .pdbqt file. The same process was applied to the T315I mutant protein (PDB ID 3OY3) [17].

### 2.2 Preparation of Ligand Files

Two-dimensional (2D) structures of the analogues and controls were drawn using the 2018 Freeware version of ACD/ChemSketch [18,19]. All structures containing the *N*-methylpiperazine moiety were drawn in their *N*4 protonated forms. The initial conformations were optimized using *Clean Structure*, *Add Explicit Hydrogens*, and *3D Optimization*, then saved as .mol files.

Additionally, co-crystallized ligands present in the PDB models were prepared for redocking. Using ADT, nilotinib and AP24589 were extracted as .pdbqt files from 3CS9 and 3OY3, respectively, then converted to .mol through Open Babel 2.4.1 [20]. Each file was opened in ChemSketch for the addition of explicit hydrogens and 3D Optimization, then saved as .mol.

All .mol files were converted to .mol2, then opened in ADT as ligands to merge nonpolar hydrogens, add Gasteiger charges, and select rotatable bonds. The processed ligands were saved as .pdbqt files.

### 2.3 Molecular Docking of Known Inhibitors and Ponatinib Analogues

Grid boxes were positioned to sufficiently cover the ATP-binding site. Grid calculations for each ligand-protein pair were followed by docking calculations using AutoDock 4.2.6, where Lamarckian Genetic Algorithm (GA) was utilized to search for the best ligand conformations. The number of GA runs was set to 500 while all other parameters were set to default [16,21,22]. ADT and BIOVIA Discovery Studio Visualizer v21.1.0.20298 were then used for viewing, calculation of root-mean-square deviation (RMSD), and detection of ligand-protein interactions [23].

### 2.4 Drug-likeness Profiling

The analogues were subjected to physicochemical and pharmacokinetic profiling through SwissADME [24]. Simplified molecular-input line-entry system (SMILES) strings were generated from the .mol files in section 2.2, and were entered in the SMILES input box.

### 2.5 Molecular Dynamics of Top Analogues

The MD simulations were performed through GROMACS 2023.2 [25] using the July 2022 version of CHARMM36 all-atom force field [25-31], following the workflow presented in the work of Dr. Justin Lemkul [32]. The protein .pdbqt files used for docking were refined in UCSF Chimera 1.17.3 [33]. Gaps due to missing amino acid residues in the 3CS9 model was repaired through an integrated Modeller interface [34,35]. Respective topologies of all proteins were then written through pdb2gmx of the GROMACS package. CHARMM-modified TIP3P water model was chosen over other models since it complements the CHARMM36 all-atom force field applied to the proteins. The *N*- and *C*- termini were set to NH3+ and COO-, respectively.

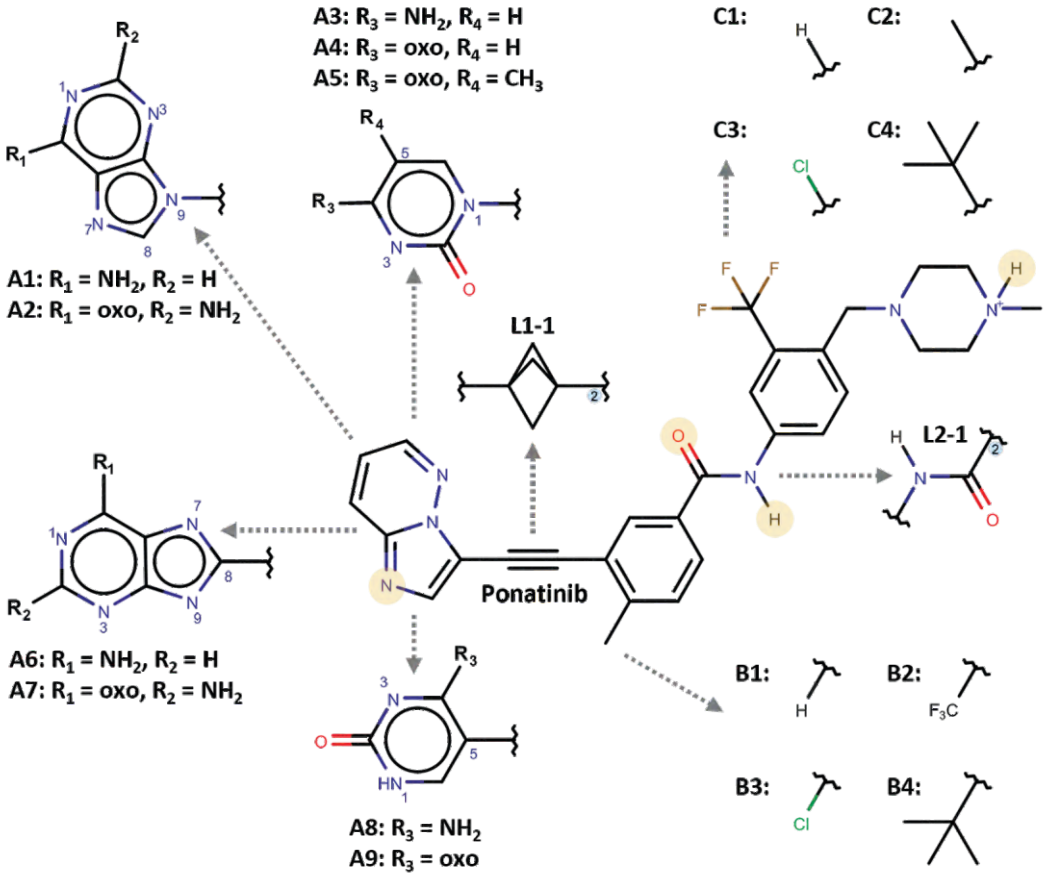


Structures in this figure were drawn using MarvinSketch 22.11.0 (https://www.chemaxon.com)

**Figure 1.** Modifications in the structure of ponatinib

Top analogues were selected based on their docking and drug-likeness profiling results. Best ligand poses from the docking simulations were extracted as .pdbqt from AutoDock4 .dlg files. Using Avogadro 1.2.0 [36], explicit hydrogens were added to the ligand structures which were then saved as .mol2 files. The files were uploaded to the CHARMM General Force Field (CGenFF) server (https://cgenff.silcsbio.com/initguess/) which uses CGenFF version 4.6 for ligand parameterization. The resulting toppar stream files (.str) were converted to GROMACS format using a script with Python 3.8.17 and NetworkX 2.3 dependencies [37].

The coordinates of each protein-ligand pair were combined in a .gro file, followed by the insertion of ligand information into the system topology. The complexes were then placed in separate rhombic dodecahedral unit cells and solvated using the SPC216 water model. Sodium ($Na^+$) ions were subsequently added as counterions to achieve system neutrality. It is also at this stage that a system is considered complete since it already has the necessary components.

Each system was then subjected to energy minimization, followed by equilibration. Minimization is achieved when the maximum force is less than 1000 $kJ{\cdot}mol^{-1}{\cdot}nm^{-1}$. Prior to equilibration, a position restraint for the ligand was inserted into the system topology. Furthermore, the system was divided into two temperature coupling groups: the complex (Protein_Ligand) and the solvent (Water_and_ions). The system was subjected to a 100-ps phase 1 canonical (NVT) ensemble equilibration with 2-fs steps, where the number of particles, volume, and temperature are constant. The output of which was subjected to phase 2 isothermal-isobaric (NPT) ensemble equilibration, which is the same as NVT but with constant pressure instead of volume. Finally, equilibrated systems were subjected to short 100-ns (100000-ps) production MD runs with 2-fs steps. All simulations were performed at 310 K (~ 37°C) [32].

### 2.6 Post Dynamics Free Energy Calculations

Molecular dynamics simulation trajectories were recentered and rewrapped to the protein backbone of the complex in the initial frame. Free energies of the fitted trajectories were calculated with Molecular Mechanics/Poisson-Boltzmann Surface Area (MMPBSA) method and its Generalized-Born counterpart (MMGBSA) through gmx_MMPBSA [38,39]. Intervals were set to 1 and 10 for MMGBSA and MMPBSA calculations, respectively. A temperature of 310.15 K was specified in both methods to account for normal body temperature.

# Results and Discussion

### 3.1 Redocking of Co-crystallized Ligands

Present in the binding site of 3CS9 is nilotinib, while AP24589 is in 3OY3. These ligands were extracted from their respective PDB models, processed as stated in section 2.2, and docked to the processed proteins. A 46 by 44 by 34 grid box centered at 28.375*x*–4.103*y*–51.782*z* was used for 3CS9, while a 62 by 34 by 28 box at 16.540*x*–6.904*y*–2.762*z* was used for 3OY3; the distance between consecutive points was set to 0.375Å. Each docking simulation resulted in 500 docked conformations, where each conformation represents one of the possible orientations of the compound when it binds to the specified site in enzyme. These conformations are automatically clustered by ADT, in which poses with similar docked orientations and binding energies are grouped into the same cluster.

Redocking of nilotinib to 3CS9 gave out 15 clusters, with the best energy cluster consisting of 138 conformers (27.6%). Relative to the co-crystallized nilotinib, the top 5 redocked poses exhibited an average RMSD of 1.201 ±0.139 Å. While cluster 1 is the top cluster in terms of energy, cluster 5 is the largest with 156 conformers (31.2%). The top 5 poses in this cluster, however, exhibited an average RMSD of 11.929 ±0.192 Å. Such high RMSD can be attributed to the flipped orientation of cluster 5 conformers. As for 3OY3, both neutral and *N*4-protonated forms of AP24589 were subjected to redocking. Both resulted in 8 clusters each, where the best energy clusters are also the largest. The top cluster from the neutral ligand consists of 420 conformers (84.0%), with a top 5 average RMSD of 0.976 ±0.244 Å. Meanwhile, the protonated form top cluster has 455 conformers (91.0%) with a top 5 average RMSD of 1.294 ±0.046 Å, proving that the crystal pose of the ligand can be reproduced even when the *N*4 of its piperazine is protonated; the protonated piperazine is crucial in forming hydrogen bonds with the acyl O's of Ile360 and His361.

### 3.2 Docking Scores

In molecular docking, lower free energies of binding (ΔG) typically indicate stronger and more favorable binding affinities, suggesting that a ligand is more likely to effectively bind to the target. However, better binding energies do not always translate to better experimental and clinical results. Case in point, the binding energies in Table 1 suggest that imatinib is more potent than nilotinib, contrary to the cellular assay $IC_{50}$ values reported in the work of Rossari and colleagues [9]. Considering the AutoDock4 standard error of 2-3 kcal/mol, the energy differences of the positive controls alone are not enough to claim that one compound is more potent than another [16]. As such, we also employed the use of cluster size-weighted scores as an alternative approach to assess the potential activity of the test compounds. This value, referred to as 'affinity score' in this paper, is calculated by multiplying the free energy of binding to the cluster size then dividing the result by 500 — the total number of conformations per simulation. It should be noted that both binding energy and affinity score were used to screen the analogues of ponatinib.

### 3.3 Single Modifications

Ponatinib analogues were generated by altering the structure of the parent compound one part at a time, as shown in Figure 1. First, the imidazo[1,2*b*]pyridazine (Ring A) was replaced with nucleobases. Purine bases — adenine and guanine — were connected to the ethynyl linker either at their *N*9 or *C*8 positions, while pyrimidines — cytosine, uracil, and thymine — were connected via their *N*1 or *C*5 positions. Next, the methyl substituent of Ring B was replaced by hydrogen, trifluoromethyl, chlorine, or *tert*-butyl group. The same approach was applied to the trifluoromethyl group of ring C, except for the second analogue where methyl was used. Lastly, the ethynyl linker (L1) was replaced by a bicyclo[1.1.1]pentyl bridge while amide linker (L2) was changed to its inverse. Docking scores of these analogues towards the wild-type and T315I mutant models are shown in Table 1. These averages were calculated from the top 1% of the 500 docked conformers of each ligand.

#### 3.3.1 Ring A Modifications

Among the nine ring A analogues, those that contain adenine and cytosine (A1, A3, A6, and A8) consistently exhibited promising binding energies and affinity scores in both protein models. Notably, the adenine(*N*9)-substituted A1 shows slightly although not significantly better scores than ponatinib. The performance of these analogues can be attributed to the presence of primary amines which acts as a hydrogen bond donor [13]. As shown in Figure 2, the 6- and 4-amino groups of A1 and A3 form a hydrogen bond with the acyl *O* of Met318, similar to that of AP24589 carboxamide [13]. While this H-bond with Met318 is absent in A6 and A8, the adenine(*C*8)-substituted analogue forms one with the phenol *O* of Tyr253 while the cytosine(*C*5) derivative interacts with Glu316 acyl *O*. The reported H-bond with Met318 *NH* is also present in these four ring A analogues, on top of various *pi* interactions of the purine and pyrimidine rings with different amino acid residues in the binding pocket.

On the other hand, some of the remaining Ring A analogues exhibited binding energies that are worse by at least 3 kcal/mol than ponatinib, such as A7 in the wild-type model, and A2, A4, and A5 in the T315I mutant. These guanine-, uracil-, and thymine-substituted analogues also showed poor performance in terms of affinity scores. For both A2 and A7, their successful formation of H-bonds with Met318 and Glu316 of 3CS9 pushed the analogues towards the direction of His361, resulting in the weakening of their other binding interactions. The second H-bond, however, was not detected in the docked pose of A7 in 3OY3. Worse, in the case of A2, the lowest energy bound conformation of this guanine(*N*9)-substituted analogue in 3OY3 exhibited a flipped orientation, similar to the cluster 5 poses of redocked nilotinib in section 3.1. The same orientation was also exhibited by pyrimidine-substituted analogues A4 and A5 in the T315I mutant model.

#### 3.3.2 Rings B and C Modifications

During the development of imatinib, it was observed that placing a methyl substituent on its ring B equivalent at a para position relative to the amide reduces its affinity towards other kinases such as protein kinase C, making it more specific for BCR-ABL tyrosine kinase. The trifluoromethyl group of ring C meta to the amide was only added until the discovery of nilotinib. This resulted in additional hydrophobic interactions with the pocket, contributing

**Table 1.** Docking scores of co-crystallized, control, and designed ligands towards BCR-ABL protein models

| Ligand | Binding Energy (kcal/mol) | | | | Affinity Score (kcal/mol) | | | |
|---|---|---|---|---|---|---|---|---|
| | 3CS9 | | 3OY3 | | 3CS9 | | 3OY3 | |
| | Score | Rank | Score | Rank | Score | Rank | Score | Rank |
| **Redocking – Nilotinib** | | | | | | | | |
| Cluster 1 | -14.49 ±0.01 | | | | -4.00 ±0.00 | | | |
| Cluster 5 | -11.05 ±0.08 | | | | -3.45 ±0.03 | | | |
| **Redocking – AP24589** | | | | | | | | |
| Protonated | | | -15.39 ±0.07 | | | | -12.93 ±0.06 | |
| Neutral | | | -16.00 ±0.03 | | | | -14.56 ±0.03 | |
| **Control** | | | | | | | | |
| Imatinib | -14.00 ±0.32 | 2 | -14.24 ±0.07 | 2 | -0.98 ±0.02 | 3 | -4.01 ±0.02 | 3 |
| Nilotinib | -13.32 ±0.13 | 3 | -12.02 ±0.03 | 3 | -3.94 ±0.04 | 2 | -4.69 ±0.01 | 2 |
| Ponatinib | -14.28 ±0.13 | 1 | -15.51 ±0.05 | 1 | -10.85 ±0.10 | 1 | -14.58 ±0.04 | 1 |
| **Single Modification – Ring A Analogues** | | | | | | | | |
| A1/VP10000 | -14.67 ±0.02 | 1 | -16.41 ±0.01 | 1 | -10.97 ±0.01 | 1 | -16.02 ±0.01 | 1 |
| A2/VP20000 | -12.57 ±0.20 | 7 | -12.17 ±0.03 | 7 | -2.04 ±0.03 | 9 | -5.28 ±0.01 | 9 |
| A3/VP30000 | -13.12 ±0.10 | 5 | -15.81 ±0.02 | 2 | -9.26 ±0.07 | 4 | -15.33 ±0.01 | 2 |
| A4/VP40000 | -12.67 ±0.06 | 6 | -11.75 ±0.04 | 9 | -7.22 ±0.03 | 7 | -8.91 ±0.03 | 8 |
| A5/VP50000 | -13.15 ±0.07 | 4 | -11.96 ±0.02 | 8 | -5.89 ±0.03 | 8 | -10.07 ±0.02 | 7 |
| A6/VP60000 | -13.47 ±0.02 | 3 | -14.69 ±0.01 | 6 | -10.29 ±0.01 | 2 | -14.19 ±0.01 | 4 |
| A7/VP70000 | -11.15 ±0.19 | 9 | -15.13 ±0.01 | 4 | -7.40 ±0.13 | 6 | -13.31 ±0.01 | 6 |
| A8/VP80000 | -13.60 ±0.04 | 2 | -15.77 ±0.03 | 3 | -9.71 ±0.03 | 3 | -14.50 ±0.02 | 3 |
| A9/VP90000 | -12.41 ±0.14 | 8 | -14.69 ±0.03 | 5 | -8.16 ±0.09 | 5 | -13.96 ±0.03 | 5 |
| **Single Modification – Linker 1 Analogue** | | | | | | | | |
| L1-1/VP01000 | -14.65 ±0.11 | | -16.22 ±0.02 | | -8.32 ±0.06 | | -13.72 ±0.02 | |
| **Single Modification – Ring B Analogues** | | | | | | | | |
| B1/VP00100 | -14.63 ±0.04 | | -15.56 ±0.04 | | -11.61 ±0.03 | | -14.96 ±0.04 | |
| B2/VP00200 | -14.12 ±0.10 | | -16.13 ±0.02 | | -8.62 ±0.06 | | -13.58 ±0.01 | |
| B3/VP00300 | -14.51 ±0.08 | | -16.49 ±0.01 | | -10.73 ±0.06 | | -15.21 ±0.01 | |
| B4/VP00400 | -13.23 ±0.12 | | -16.03 ±0.05 | | -2.78 ±0.02 | | -7.21 ±0.02 | |
| **Single Modification – Linker 2 Analogue** | | | | | | | | |
| L2-1/VP00010 | -14.62 ±0.07 | | -15.43 ±0.07 | | -12.07 ±0.06 | | -14.59 ±0.07 | |
| **Single Modification – Ring C Analogues** | | | | | | | | |
| C1/VP00001 | -14.51 ±0.04 | | -15.79 ±0.02 | | -13.41 ±0.03 | | -15.66 ±0.02 | |
| C2/VP00002 | -14.83 ±0.05 | | -16.43 ±0.01 | | -12.73 ±0.04 | | -16.30 ±0.01 | |
| C3/VP00003 | -14.94 ±0.02 | | -16.58 ±0.01 | | -12.79 ±0.01 | | -16.31 ±0.01 | |
| C4/VP00004 | -15.28 ±0.02 | | -17.31 ±0.01 | | -11.65 ±0.02 | | -16.06 ±0.01 | |
| **Combinatorial Modifications – Top Analogues** | | | | | | | | |
| VP10004 | -14.99 ±0.04 | 52 | **-17.09 ±0.06** | 1 | -11.57 ±0.03 | 72 | **-16.68 ±0.06** | 1 |
| VP10312 | -14.83 ±0.03 | 62 | -16.10 ±0.01 | 35 | **-14.74 ±0.03** | **9** | **-16.10 ±0.01** | **9** |
| VP81014 | **-16.58 ±0.03** | 2 | **-16.25 ±0.02** | 20 | -15.36 ±0.03 | 2 | -13.26 ±0.02 | 131 |
| VP81114 | **-16.65 ±0.03** | 1 | -15.35 ±0.13 | 131 | -6.36 ±0.01 | 244 | -4.54 ±0.04 | 313 |
| VP81310 | -16.15 ±0.01 | 6 | -15.24 ±0.01 | 153 | **-15.66 ±0.01** | 1 | -13.47 ±0.01 | 123 |
| VP81314 | -16.25 ±0.03 | **4** | -16.42 ±0.01 | **12** | -14.40 ±0.03 | 18 | -14.22 ±0.01 | 87 |

to the latter drug's activity against certain mutations of the target [9,12]. Our docking simulations of ponatinib show that the methyl group indeed interacts with the alkyl side chains of Val256, Ala269, and Lys271 in 3CS9. The trifluoromethyl also shows similar hydrophobic interactions with Leu298, Val299, Val379, and His361. Halogen bonds with Val379 and Ala380 acyl *O*'s were also detected. Furthermore, the fluorine atoms also exhibited a nonconventional C-H hydrogen bond with the Ala380 alpha-hydrogen, and a conventional one with His361 *NH*.

Docking simulations of the simplified analogues—B1 and C1—show that other parts of the analogue can compensate for the lost interactions. Case in point, ring B of B1 shifted towards the phenyl ring of Phe382 resulting in a T-shaped *pi-pi* interaction, while ring C of C1 formed a *pi*-anion interaction with Aps381 carboxylate.

The next strategy in line involved swapping the isosteric hydrogen and fluorine atoms between the methyl and trifluoromethyl groups. The trifluoromethyl-containing B2 exhibited halogen bonds with Ala269 acyl *O*, Val270 acyl *C*, Lys271 *NH*, Ile313 acyl *O*, and Thr315 *NH*. The fluorine atoms are also capable of acting as acceptors for the H-bond donors in this list. These interactions resulted in comparable binding energies but poorer affinity scores than the parent compound. In the case of C2, replacing the fluorine atoms of the ring C trifluoromethyl resulted in the loss of halogen and hydrogen bonds, although docking scores indicate that the rest of the molecule compensated for it.

Third is the use of chlorine as an isosteric replacement for trifluoromethyl. Docked poses of B3 show that the chlorine atom can form hydrophobic interactions with the same residues that the methyl group of ponatinib

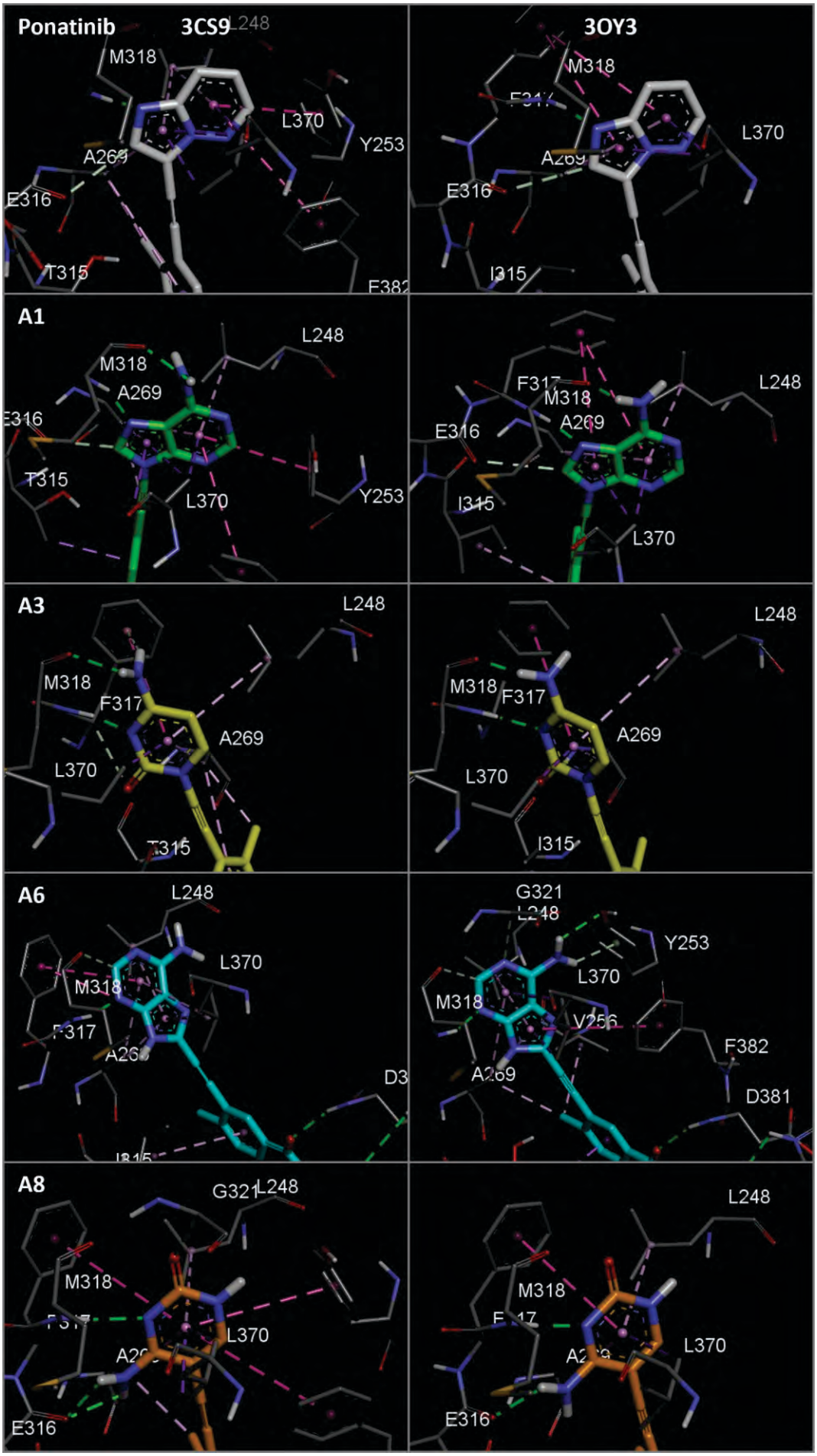


**Figure 2.** Binding interactions of top ring A analogues

originally interacted with. For C3, the chloro substituent was not enough to reproduce the polar interactions of ponatinib's trifluoromethyl group, although its alkyl interactions were still detected in 3OY3. In the case of C3-3CS9 complex, chlorine did not show any interactions but the phenyl ring to which it is attached to form a *pi*-anion interaction with Asp381. In general, B3 and C3 exhibited good docking scores.

Lastly, the substituents were converted to a *tert*-butyl group. Due to its bulky nature, placing it in ring B pushed the phenyl ring towards Val299, resulting in an additional *pi*-alkyl interaction with the side chain of the residue. The *tert*-butyl itself formed three alkyl interactions with the same residues as ponatinib in 3CS9, while the interaction with Val256 was replaced by Ile315 in 3OY3. These interactions are reflected in the B4's good binding energies, however, not in its affinity scores. On the other hand, placement of this group ring C resulted in less alkyl interactions. Still, C4 exhibited good docking scores, probably since other parts of the analogue such as ring B and the 4-(methylpiperazin-1-yl)methyl appear to have formed beneficial interactions.

#### 3.3.3 Linker Modifications

Ponatinib contains two linkers: an ethynyl and an amide. The first one serves as a connector for imidazo[1,2*b*]pyridazine and phenyl ring B. The sp hybridization of its carbons ensures that the *N*-heterocycle and the methylphenyl are properly oriented towards their respective binding pockets. Ethenyl, which is $sp^2$ hybridized, was also considered during the discovery of ponatinib, however, it was established that a straight-line connectivity is crucial for the drug's ability to evade the steric effects of Ile315 in the T315I mutant [8]. For the first linker modification, ethynyl was changed to one of its bioisosteres — bicyclo[1.1.1]pentyl [40]. No interactions were detected between the BCR-ABL binding site and the original linker. On the other hand, replacement with bicyclopentyl resulted in alkyl interactions with the alkyl side chains of Val256, Ala269, and Val299, and the phenyl ring of Phe382 in 3CS9. While no interactions were observed between L1-1 and 3OY3, there were also no detected repulsive interactions with Ile315.

The second linker is an amide that Phenyl rings connected by a secondary amide linker is a recurring theme in the structures of ponatinib and its precursors. Although there is a slight difference in the case of imatinib where the amide is in an inverted position. Docking of L2-1 which contains the same inverted secondary amide resulted to the same H-bonds of the acyl *O* with Asp381 *NH*, and of the amide *NH* with Glu286 carboxylate and Met290 *S*. In terms of docking scores, both bicyclopentyl and inverse amide performed well, suggesting that they may be considered especially when one offers a simpler synthetic approach.

### 3.4 Combinatorial Modifications

#### 3.4.1 Molecular Docking

Among the first set of analogues, adenine- and cytosine-substituted compounds were subjected to further derivatization using all possible combinations of unchanged and modified ring B, ring C, and linkers. A five-digit code was then applied to these analogues, with each digit representing a part of ponatinib as discussed in the previous section. This led to 100 possible combinations for each ring A analogue, resulting in a total of 400 analogues.

The analogues were first screened using the binding energies and affinity scores of ponatinib as cut-off values, and then ranked using these same parameters. In terms of binding energy, 138 are better than ponatinib in 3CS9, 113 in 3OY3, and only 55 in both. Based on affinity scores, the number of analogues are 92, 69, and 33, respectively. Most of which are from the derivatives of A1, with A6 derivatives on the other end of the spectrum. These analogues were then ranked based on either the sum of their docking scores or the sum of their rankings in each model. For the latter, the best theoretical value is 2 if the analogue ranked the best in both models. The overall top analogues with combinatorial modifications listed in Table 1 were then subjected to molecular dynamics simulations. The adenine-substituted analogue VP10004 has a ring C *tert*-butyl substituent, while VP10312 has a ring B chloro group, a ring C methyl group, and an inverted amide linker. The four selected cytosine-substituted analogues have bicyclopentyl and inverted amide linkers, three of which have a ring C *tert*-butyl group: VP81114 has a demethylated ring B, VP81314 has a ring B chloro group, and VP81014 lacks a modification in the said ring. Lastly, VP81310 is a form of VP81314 without the ring C modification.

#### 3.4.2 Short Molecular Dynamics

Complexes formed by ponatinib and the top 6 selected analogues with 3CS9 and 3OY3 from the previous section underwent 100-ns MD simulations. To assess their stability during this period, we calculated three types of complex RMSDs — t=0, Δt=5ns, and Δt=10ns — from non-hydrogen atoms of each protein backbone and ligand. RMSD (t=0), or simply RMSD, measures the difference of each frame in the trajectory relative to its initial frame. Obtained using the *-prev* option of the *gmx* rms package, $RMSD_{\Delta 5}$ and $RMSD_{\Delta 10}$ show how frames differ from their state 5 or 10 nanoseconds ago [41]. An RMSD of 3.0Å typically accepted as the upper limit of structural similarity between two protein conformations [42]. However, it should not be treated as a strict cut-off since chain length can easily affect protein flexibility [43-45]. For proteins containing ~250 residues, an RMSD of 5.0Å may still be acceptable [46].

Complexes involving the wild-type model showed lower RMSDs than their T315I mutant counterparts (Figure 3). All 3CS9 complexes maintained RMSDs below 3.0Å throughout their trajectories, except for those with VP81014 and VP81310, where 1.97% and 2.24% of 10,001 frames fell within the 3.0-4.0Å range. VP10312-3CS9 showed the most stable trajectory, with 99.70% of frames having an RMSD of ≤ 2.0Å. In contrast, its complex with the T315I mutant spent most of its trajectory (61.54%) in the 3.0-4.0Å range, and 6.22% between 4.0-5.0Å. It has the second highest RMSD profile among 3OY3 complexes, next to ponatinib-3OY3 with 54.40%, 20.24%, and 1.01% of frames falling within the 3.0-4.0Å, 4.0-5.0Å, and 5.0-6.0Å RMSD ranges, respectively. VP81014 displayed the most stable trajectory among the mutant complexes, with 86.50% below 3.0Å.

Moving RMSDs of 3CS9 complexes were predominantly under 2.0Å, indicating good structural similarity between frames separated by 5- and 10-ns intervals [47]. Conversely, several "peaks" were observed in $RMSD_{\Delta 5}$ and $RMSD_{\Delta 10}$ plots of 3OY3 complexes, particularly those involving VP81310 and VP10312. The root-mean-square-fluctuation (RMSF) plot of VP10312-3OY3 revealed a highly flexible activation loop (A-loop), which could explain its RMSD profile (Figure 3). However, VP81310 showed minimal fluctuations in its RMSF plot, suggesting that its RMSD might be attributed to terminal residues of 3OY3; notably, 3OY3 contains 5 and 11 more residues than 3CS9 at its *N*- and *C*-termini, respectively [15-17].

The A-loop plays an important role in the activity of BCR-ABL kinases. At the start of the A-loop lies the DFG-motif, where its Asp381 carboxylate forms a hydrogen bond with the amide *NH* of the inhibitor, maintaining the kinase in its DFG-out or inactive conformation. Another functionally-relevant residue within this loop is Arg386, whose guanidinium group can form a salt bridge with Glu286 to prevent peptide substrate binding [12]. This Glu286 in the αC helix can also form a salt bridge with Lys271 of the β3 sheet and a hydrogen bond with the amide *O* of the inhibitor — competing interactions that explain the observed fluctuations for the A-loop, β3 sheet, and αC helix residues [48].

To assess the potential impact of these movements on enzyme inhibition, distances between atoms specified by Paul and colleagues were measured. An inactive kinase typically exhibits a kinked P-loop (< 9Å), a DFG motif in the out conformation (> 10Å), a salt bridge between the A-loop and αC helix (< 4Å), and the absence of one between the β3 sheet and αC helix (> 4Å). These latter two parameters describe an αC helix interacting with the A-loop instead of the β3 [49,50]. In contrast, the PDB-native states of both 3CS9 and 3OY3 exhibit the opposite, despite being models of inhibited enzymes (Table 2). Similar observations were made for all complexes except for five, where the Glu286---Lys271 salt bridge appears unstable. These deviations in Glu286 interactions can be attributed to its H-bond with the inhibitor's amide linker. Regarding P-loop states, only VP81114-3OY3 displayed an extended conformation, while the rest exhibited kinked conformations. Most importantly, all complexes maintained their DFG-out conformations throughout the 100-ns simulation. Even with an open A-loop and an extended P-loop, the kinase remains inhibited because the ligand prevents the DFG-motif from coordinating with the catalytic magnesium ($Mg^{2+}$) ions [12].

We also monitored ligand RMSDs to assess the behavior of analogues within the binding site. For small molecules, a 2.0Å RMSD is commonly used as an upper threshold for structural similarity [51,52]. Figure 3 indicates that most ligands have RMSDs (t=0) above this limit, particularly the cytosine-substituted analogues. These values, together with their moving

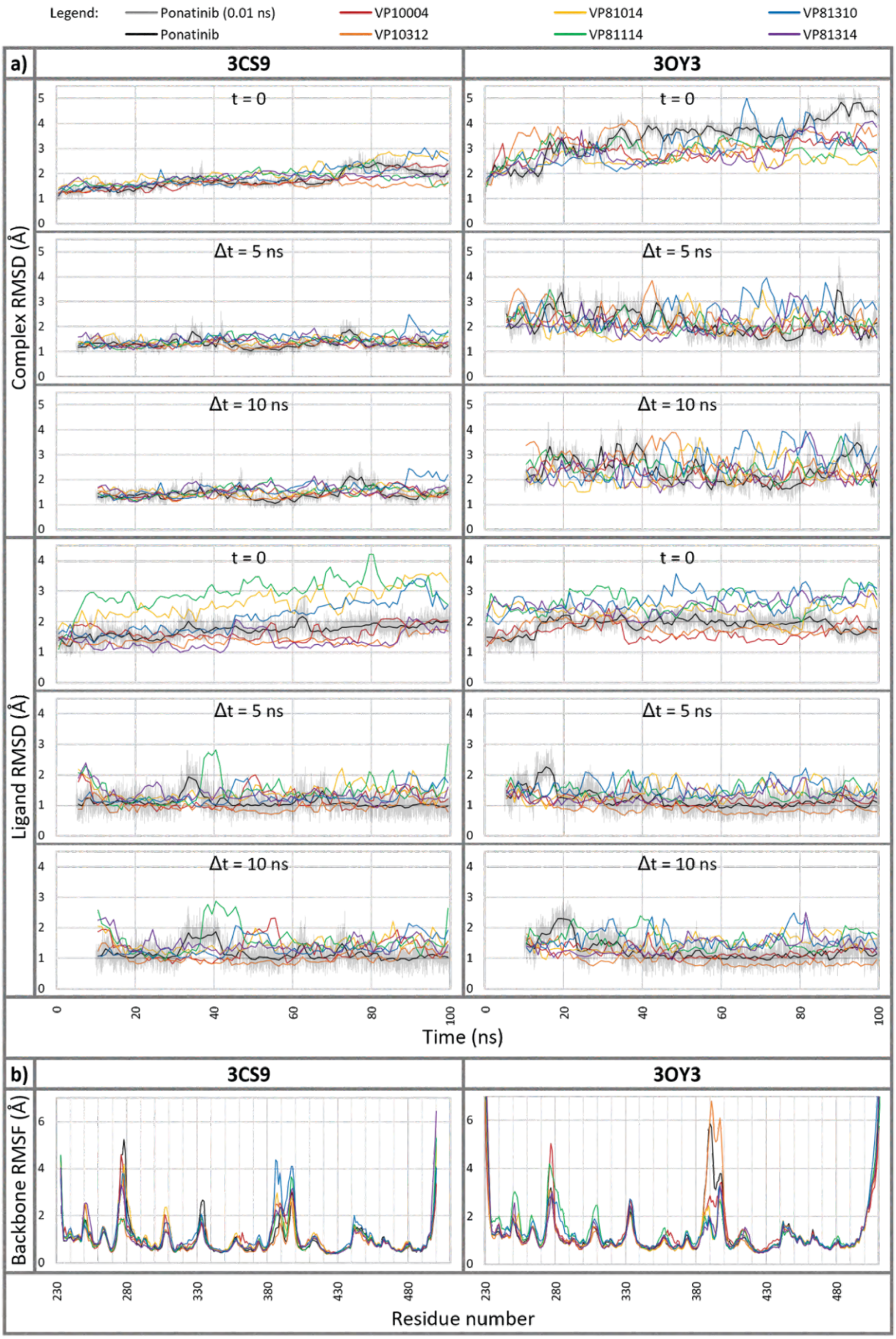


a) RMSD plots. For better visualization, all plots were constructed using the average RMSDs in each 1-ns interval, except for Ponatinib (0.01 ns) which represents the individual RMSDs of each frame. b) RMSF plots. Key structural domains within the target protein are as follows: P-loop (248-253), β3 sheet (266-272), αC helix (280-292), β4 sheet (301-305), β5 sheet (312-316), αD helix (323-329), αE helix (337-357), activation loop (381-405), αF helix (418-434), αG helix (445-454), and αH helix (466-475) [15,17,61].

**Figure 3.** Trajectory RMSDs and RMSFs of the ligand-protein complexes

**Table 2.** 100-ns average distances between selected atoms of 3CS9 and 3OY3 complexes

| Ligand | Distance (Å) | | | | | | | |
|---|---|---|---|---|---|---|---|---|
| | 3CS9 | | | | 3OY3 | | | |
| | P-loop | DFG motif | A-loop---αC | β3---αC | P-loop | DFG motif | A-loop---αC | β3---αC |
| Native | 6.20 | 11.55 | **10.80** | **3.72** | 6.45 | 11.37 | **10.86** | **3.86** |
| Ponatinib | 6.87 ±0.94 | 12.05 ±0.92 | **8.55** ±2.62 | **3.72** ±4.93 | 6.49 ±0.70 | 12.03 ±0.70 | **8.84** ±0.90 | **3.65** ±0.60 |
| VP10004 | 6.81 ±1.25 | 12.14 ±0.69 | **10.77** ±3.62 | **3.78** ±2.49 | 6.40 ±0.71 | 12.00 ±0.67 | **9.33** ±1.10 | **3.63** ±0.85 |
| VP10312 | 6.66 ±0.84 | 12.22 ±0.70 | **10.58** ±2.33 | 4.23 ±2.38 | 6.25 ±0.90 | 11.90 ±0.59 | **7.41** ±1.36 | **3.51** ±0.45 |
| VP81014 | 7.87 ±1.53 | 12.56 ±0.84 | **11.10** ±2.28 | 4.42 ±1.88 | 5.45 ±0.76 | 13.13 ±0.85 | **11.37** ±1.86 | **3.55** ±0.77 |
| VP81114 | 6.23 ±0.79 | 12.85 ±1.05 | **9.09** ±2.18 | 4.28 ±4.14 | **9.44** ±1.80 | 12.72 ±0.73 | **8.94** ±1.24 | 8.14 ±2.98 |
| VP81310 | 6.09 ±0.73 | 12.48 ±0.75 | **13.95** ±3.75 | **3.72** ±3.02 | 6.04 ±1.03 | 12.18 ±0.99 | **12.47** ±0.73 | 4.68 ±1.60 |
| VP81314 | 6.08 ±1.22 | 12.64 ±1.00 | **12.89** ±2.97 | **3.62** ±2.12 | 6.98 ±1.39 | 12.58 ±0.62 | **7.57** ±0.76 | **3.80** ±0.97 |

**Table 3.** Binding free energies and RMSDs of BCR-ABL complexes

| Ligand | Binding Free Energy (kcal/mol) | | Root Mean Square Deviation (Å) | | | |
|---|---|---|---|---|---|---|
| | MMGBSA | MMPBSA | Complex | | Ligand | |
| | Ave ±SD | Ave ±SD | t=100ns | Ave ±SD | t=100ns | Ave ±SD |
| Wild-type Kinase (3CS9) | | | | | | |
| Ponatinib | -54.91 ±4.26 | -44.73 ±5.09 | 1.955 | 1.733 ±0.352 | 1.763 | 1.710 ±0.266 |
| VP10004 | -52.78 ±4.73 | -40.49 ±7.70 | 2.491 | 1.694 ±0.347 | 2.171 | 1.647 ±0.283 |
| VP10312 | -51.72 ±5.88 | -36.56 ±6.72 | 1.718 | 1.543 ±0.166 | 1.531 | 1.369 ±0.237 |
| VP81014 | -50.23 ±4.68 | -38.29 ±5.76 | 2.844 | 2.056 ±0.439 | 3.445 | 2.638 ±0.552 |
| VP81114 | -51.20 ±4.48 | -38.88 ±5.58 | 1.562 | 1.829 ±0.296 | 2.809 | 2.962 ±0.559 |
| VP81310 | -50.54 ±7.02 | -36.47 ±7.39 | 2.607 | 1.883 ±0.464 | 3.073 | 2.143 ±0.579 |
| VP81314 | -48.42 ±6.91 | -34.11 ±7.21 | 2.286 | 1.795 ±0.216 | 2.603 | 2.200 ±0.294 |
| T315I Mutant Kinase (3OY3) | | | | | | |
| Ponatinib | -56.82 ±3.69 | -41.64 ±5.55 | 4.193 | 3.442 ±0.788 | 1.796 | 1.889 ±0.280 |
| VP10004 | -52.85 ±4.34 | -43.20 ±4.89 | 3.330 | 2.906 ±0.419 | 2.189 | 1.645 ±0.326 |
| VP10312 | -50.26 ±3.38 | -30.09 ±7.67 | 3.761 | 3.214 ±0.568 | 1.618 | 1.778 ±0.273 |
| VP81014 | -55.97 ±5.60 | -45.94 ±6.31 | 2.368 | 2.564 ±0.373 | 2.723 | 2.342 ±0.334 |
| VP81114 | -43.15 ±3.74 | -31.64 ±6.11 | 2.843 | 2.933 ±0.429 | 2.981 | 2.658 ±0.444 |
| VP81310 | -48.89 ±5.03 | -37.36 ±5.61 | 2.940 | 2.968 ±0.712 | 2.888 | 2.694 ±0.428 |
| VP81314 | -55.05 ±5.56 | -41.03 ±7.73 | 4.005 | 2.802 ±0.603 | 2.999 | 2.514 ±0.343 |

RMSDs which are generally < 2.0Å, suggest that ligands initially diverge from their initial poses but subsequently adopt more stable conformations. The $RMSD_{\Delta 5}$ and $RMSD_{\Delta 10}$ plots of 3CS9-bound ligands revealed structural transitions, notably in VP81114 at around 37-ns. Concurrently, a reduction in ligand hydrogen bonding with 3CS9 was observed (Figure 4). Further inspection confirmed that the piperazine *N*4 moved away from His361, resulting in the loss of its H-bond with the residue. Other 3CS9- and 3OY3-bound ligands also exhibited similar transitions involving the piperazine ring, although the movements were away from the carboxylate group of Asp381. Meanwhile, the 3OY3-bound VP10004 showed a transition around 36-ns, with the amide *NH* moving toward Glu286 and the piperazine toward Ile360, resulting in additional H-bonds.

The most consistent H-bonds involved the inhibitor amide *O* and Asp381 *NH*, followed by those formed by ring A with the hinge region. In adenine-substituted derivatives, *N*7 of purine and its 6-amino group interacted with Met318 *NH* and acyl *O*. Cytosine-substituted derivatives also interacted with Met318 *NH* via the pyrimidine *N*3 and 2-oxo atoms. Additionally, the 4-amino substituent formed hydrogen bonds with Glu316 acyl *O* and Thr315 hydroxyl *O*. These interactions align with literature-reported findings and those observed in docking experiments [8,12,13,53,54].

According to the equations employed in the MMPBSA/MMGBSA calculations, hydrogen bonds are incorporated into molecular mechanical energy changes as electrostatic interactions [38,55]. Their effects on binding free energies (ΔG) can be intuitively observed in Figure 4, where binding improves with hydrogen bonds are formed and weakens when these interactions are disrupted. However, it should be noted that a complex with more hydrogen bonds may not always exhibit a lower energy than another with fewer H-bonds, as van der Waals forces, other electrostatic interactions, and solvation energies also contribute to the calculated ΔG [56,57]. For instance, VP10312-3CS9 and VP81014-3CS9 have comparable energies even though the latter has 1 to 2 fewer hydrogen bonds. The amount of alkyl interactions produced by the bicyclopentyl linker and ring C *tert*-butyl of VP81014 may have compensated for this difference.

Among the top analogues, VP10004 and VP81014 exhibited the best 100-ns average binding free energies with the wild-type and T315I mutant kinases, respectively (Table 3). Throughout the trajectory, VP10004 maintained H-bonds with Met318 *NH*, Met318 acyl *O*, and Asp381 *NH*, occasionally forming H-bonds with Glu286 and Asp381 carboxylates. Meanwhile, VP81014 consistently formed H-bonds with Asp381 *NH* and Glu286 carboxylate. Its piperazine ring showed less movements due to sustained H-bond with Asp381 carboxylate, Asp363 carboxylate, Ile360 acyl *O*, or His361 acyl *O*. The cytosine ring also interacted with various residues via hydrogen bonding. In addition to previously reported interactions, the following hydrogen bonding interactions of the pyrimidine were observed: *N*3 with Asn322 α-*NH*; 2-oxo substituent with Asn322 side chain *NH*, Asn322 α-*NH*, and Tyr253 phenol *OH*; *N*1 with Tyr253 acyl *O*, Tyr253 phenol *O*, Phe382 acyl *O*. Alkyl interactions of ring B methyl and ring C *tert*-butyl substituents were also observed for both ligands.

### 3.4.3 Drug-likeness Profiles

Ponatinib and its analogues were profiled using SwissADME [24]. A BOILED-Egg analysis was employed to assess the potential oral bioavailability

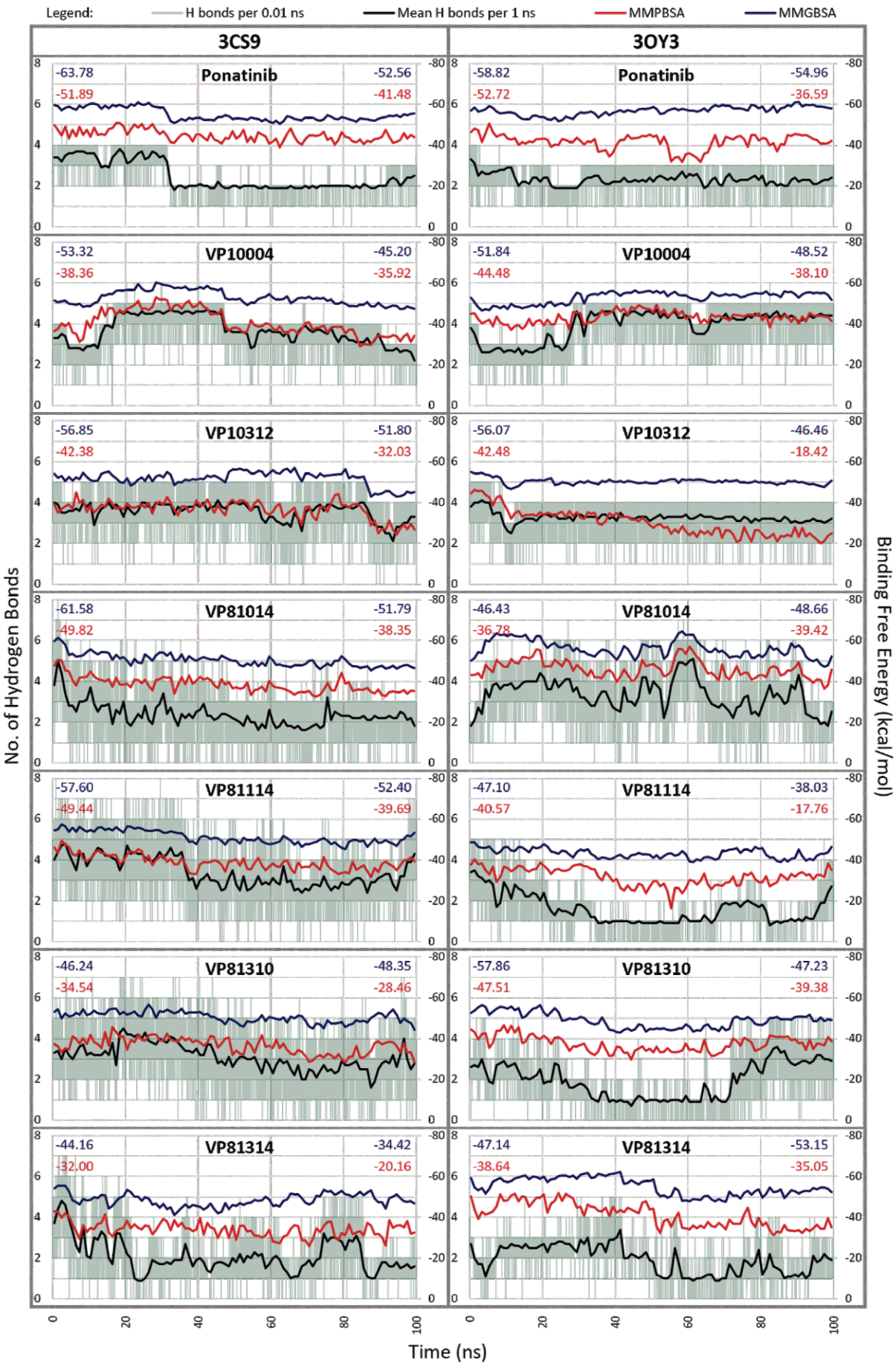


The calculated binding free energies of the first and last frames in each trajectory are shown in the upper left and upper right corners of each box, respectively.

**Figure 4.** Hydrogen bonds and binding free energies of the ligand-protein complexes

and blood-brain barrier permeation of the compounds [58]. Since ponatinib falls within the yolk, the model suggests that it can be taken orally and can enter the central nervous system; ponatinib is administered orally in tablet form and is known to have effects in the CNS [8,59,60]. Ring B, ring C, and linker analogues also fall within this region, except for C1, which is excluded due to its low log P. On the other hand, all ring A analogues, including those with combinatorial modifications and top analogues, are predicted to have good oral bioavailability, except for VP61200 and VP61210, which both fall outside the orally bioavailable region. Lastly, synthetic accessibility (SA) scores indicate that among the top analogues, VP10312 is the easiest to synthesize.

# Conclusions

This study involved the generation and analysis of 415 ponatinib analogues, which included 19 analogues with single modifications and 396 derivatives of these compounds. The investigation focused on their binding energies and conformational dynamics in two critical BCR-ABL tyrosine kinase models: 3CS9 representing the wild-type target and 3OY3 for the T315I mutant. Notably, analogues containing adenine and cytosine consistently displayed strong binding energies and affinity scores, primarily attributed to the presence of primary amines that facilitated important hydrogen bond interactions.

The exploration of various substitutions within the other two rings and linkers revealed the potential for compensatory interactions, contributing to stable binding. Short molecular dynamics simulations of the top analogues shed light on the intricate relationship between conformational changes and binding energies. Some complexes exhibited increased RMSDs due to the highly flexible A-loop; however, despite A-loop opening, all complexes remained in the inactive DFG-out conformation. Among the top analogues, VP10004 and VP81014 stood out with promising binding free energies.

Furthermore, drug-likeness predictions indicated that the majority of the analogues (413 out of 415) could be suitable for oral administration. VP10312 emerged as the most feasible analogue for synthesis among the top performers, based on synthetic accessibility scores.

To gain a more comprehensive understanding and further assess the potential of these compounds, it is recommended to conduct longer production molecular dynamics simulations with replicates, proceed with the synthesis of the top analogues, and subject them to enzyme- or cell-based assays.

# References


1. Colicelli J. (2010) ABL Tyrosine Kinases : Evolution of Function, Regulation, and Specifity. Sci. Signal. 3:1–26, doi:10.1126/scisignal.3139re6.
2. Hantschel O. (2012)Structure, Regulation, Signaling, and Targeting of Abl Kinases in Cancer. Genes and Cancer. 3:436–446, doi:10.1177/1947601912458584.
3. Manley PW, Cowan-Jacob SW, Buchdunger E, Fabbro D, Fendrich G, Furet P, Meyer T, Zimmermann J. (2002) Imatinib: A Selective Tyrosine Kinase Inhibitor. Eur. J. Cancer. 38(5):19–27, doi:10.1016/s0959-8049(02)80599-8.
4. Cowan-Jacob S, Guez V, Fendrich G, Griffin J, Fabbro D, Furet P, Liebetanz J, Mestan, J, Manley P. (2004) Imatinib (STI571) Resistance in Chronic Myelogenous Leukemia: Molecular Basis of the Underlying Mechanisms and Potential Strategies for Treatment. Mini-Reviews Med. Chem. 4:285–299, doi:10.2174/1389557043487321.
5. Iqbal N, Iqbal N. (2014) Imatinib: A Breakthrough of Targeted Therapy in Cancer. Chemother. Res. Pract. 1–9, doi:10.1155/2014/357027.
6. Kuo C.-Y, Wang P.-N, Hwang W.-L, Tzeng C.-H, Bai L.-Y, Tang J.-L, Chang M.-C, Lin S.-F, Chen T.-Y, Chen Y.-C, *et al.* (2018) Safety and Efficacy of Nilotinib in Routine Clinical Practice in Patients with Chronic Myeloid Leukemia in Chronic or Accelerated Phase with Resistance or Intolerance to Imatinib: Results from the NOVEL Study. Ther. Adv. Hematol. 9, 65–78, doi:10.1177/2040620718756603.
7. Weisberg E, Manley P.W, Breitenstein W, Brüggen J, Cowan-Jacob S.W, Ray A, Huntly B, Fabbro D, Fendrich G, Hall-Meyers E, *et al.* (2005) Characterization of AMN107, a Selective Inhibitor of Native and Mutant Bcr-Abl. Cancer Cell 7:129–141, doi:10.1016/j.ccr.2005.01.007.
8. Huang WS, Metcalf CA, Sundaramoorthi R, Wang Y, Zou D, Thomas RM, Zhu X, Cai L, Wen D, Liu S, *et al.* (2010) Discovery of 3-[2-(Imidazo[1,2- b ]Pyridazin-3-Yl)Ethynyl]-4-Methyl-N -{4-[(4-Methylpiperazin-1-Yl)Methyl]-3-(Trifluoromethyl)Phenyl}benzamide (AP24534), a Potent, Orally Active Pan-Inhibitor of Breakpoint Cluster Region-Abelson (BCR-ABL) Kinase Includin. J. Med. Chem. 53:4701–4719, doi:10.1021/jm100395q.
9. Rossari F, Minutolo F, Orciuolo E. (2018) Past, Present, and Future of Bcr-Abl Inhibitors: From Chemical Development to Clinical Efficacy. J. Hematol. Oncol. 11:1–14, doi:10.1186/s13045-018-0624-2 REVIEW.
10. Azanza JR, Sádaba B, Díez N. (2018) Comparative Pharmacology of Tyrosine Kinase Inhibitors for the Treatment of Chronic Myeloid Leukemia. Int. J. Clin. Pharmacol. Pharmacother. 3, 1–15, doi:10.15344/2456-3501/2018/134.
11. Dianne Pulte E, Chen H, Price LSL, Gudi R, Li H, Okusanya OO, Ma L, Rodriguez L, Vallejo J, Norsworthy KJ, *et al.* (2022) FDA Approval Summary: Revised Indication and Dosing Regimen for Ponatinib Based on the Results of the OPTIC Trial. Oncologist 27:149–157, doi:10.1093/oncolo/oyab040.
12. Reddy EP, Aggarwal AK. (2012) The Ins and Outs of Bcr-Abl Inhibition. Genes and Cancer 3:447–454, doi:10.1177/1947601912462126.
13. Zhou T, Commodore L, Huang WS, Wang Y, Thomas M, Keats J, Xu Q, Rivera VM, Shakespeare WC, Clackson T, *et al.* (2011) Structural Mechanism of the Pan-BCR-ABL Inhibitor Ponatinib (Ap24534): Lessons for Overcoming Kinase Inhibitor Resistance. Chem. Biol. Drug Des. 77:1–11, doi:10.1111/j.1747-0285.2010.01054.x.
14. Zabriskie MS, Eide CA, Tantravahi SK Vellore NA, Estrada J, Nicolini FE, Khoury HJ, Larson RA, Konopleva M, Cortes JE, *et al.* (2014) BCR-ABL1 Compound Mutations Combining Key Kinase Domain Positions Confer Clinical Resistance to Ponatinib in Ph Chromosome-Positive Leukemia. Cancer Cell. 26:428–442, doi:10.1016/j.ccr.2014.07.006.
15. Cowan-Jacob SW, Fendrich G, Manley P, Liebetanz J, Fabbro D. (2008) PDB Entry - 3CS9 https://www.wwpdb.org/pdb?id=pdb_00003cs9.
16. Morris GM, Huey R, Lindstrom W, Sanner MF, Belew RK, Goodsell DS, Olson AJ. (2009) AutoDock4 and AutoDockTools4: Automated Docking with Selective Receptor Flexibility. J. Comput. Chem. 30:2785–2791.
17. Zhou T, Commodore L, Huang WS, Wang Y, Thomas M, Keats J, Xu Q, Rivera V, Shakespeare WC, Clackson T, *et al.* PDB Entry - 3OY3 https://www.wwpdb.org/pdb?id=pdb_00003oy3.
18. Advanced Chemistry Development ACD/ChemSketch for Academic and Personal Use Available online: https://www.acdlabs.com/resources/freeware/chemsketch/.
19. ACD/ChemSketch (Freeware), Version 2018.2.5 2018.
20. O'Boyle NM, Banck M, James CA, Morley C, Vandermeersch T, Hutchison GR. (2011) Open Babel. J. Cheminform. 3:1–14, doi:10.1186/1758-2946-3-33.
21. Morris GM, Goodsell DS, Halliday RS, Huey R, Hart WE, Belew RK, Olson AJ. (1998) Automated Docking Using a Lamarckian Genetic Algorithm and an Empirical Binding Free Energy Function. J. Comput. Chem. 19:1639–1662, doi:10.1002/(SICI)1096-987X(19981115)19:14<1639::AID-JCC10>3.0.CO;2-B.
22. Morris GM, Goodsell DS, Pique ME, Lindstrom W, Huey R, Forli S, Hart WE, Halliday S, Belew R, Olson AJ. (2012) AutoDock Version 4.2 User Guide.
23. BIOVIA Dassault Systèmes Discovery Studio Visualizer 2020.
24. Daina A, Michielin O, Zoete V. (2017) SwissADME: A Free Web Tool to Evaluate Pharmacokinetics, Drug-Likeness and Medicinal Chemistry Friendliness of Small Molecules. Sci. Rep. 7:1–13, doi:10.1038/srep42717.
25. Abraham MJ, Murtola T, Schulz R, Páll S, Smith JC, Hess B, Lindah E. (2015) Gromacs: High Performance Molecular Simulations through Multi-Level Parallelism from Laptops to Supercomputers. SoftwareX (1–2):19–25, doi:10.1016/j.softx.2015.06.001.
26. Abraham M, Alekseenko A, Bergh C, Blau C, Briand E, Doijade M, Fleischmann S, Gapsys V, Garg G, Gorelov S, *et al.* (2023) GROMACS 2023.2 Source Code.
27. Abraham M, Alekseenko A, Bergh C, Blau C, Briand E, Doijade M, Fleischmann S, Gapsys V, Garg G, Gorelov S, *et al.* (2023) GROMACS 2023.2 Manual.

28. Vanommeslaeghe K, Prabhu Raman E, MacKerell AD. (2012) Automation of the CHARMM General Force Field (CGenFF) II: Assignment of Bonded Parameters and Partial Atomic Charges. J. Chem. Inf. Model. 52:3155–3168, doi:10.1021/ci3003649.
29. Soteras Gutiérrez I, Lin FY, Vanommeslaeghe K, Lemkul JA, Armacost KA, Brooks CL, MacKerell AD. (2016) Parametrization of Halogen Bonds in the CHARMM General Force Field: Improved Treatment of Ligand–Protein Interactions. Bioorganic Med. Chem. 24:4812–4825, doi:10.1016/j.bmc.2016.06.034.
30. Vanommeslaeghe K, Hatcher E, Acharya C, Kundu S, Zhong S, Shim J, Darian E, Guvench O, Lopes P, Vorobyov I, *et al.* (2010) CHARMM General Force Field (CGenFF): A Force Field for Drug-like Molecules Compatible with the CHARMM All-Atom Additive Biological Force Fields. J. Comput. Chem. 31:671–690, doi:10.1002/jcc.21367.CHARMM.
31. Vanommeslaeghe K, MacKerell AD. (2012) Automation of the CHARMM General Force Field (CGenFF) I: Bond Perception and Atom Typing. J. Chem. Inf. Model. 52:3144–3154, doi:10.1021/ci300363c.
32. Lemkul J. (2019) From Proteins to Perturbed Hamiltonians: A Suite of Tutorials for the GROMACS-2018 Molecular Simulation Package [Article v1.0]. Living J. Comput. Mol. Sci. (1)1–53, doi:10.33011/livecoms.1.1.5068.
33. Pettersen EF, Goddard TD, Huang CC, Couch GS, Greenblatt DM, Meng EC, Ferrin TE. (2004) UCSF Chimera - A Visualization System for Exploratory Research and Analysis. J. Comput. Chem. 25;1605–1612, doi:10.1002/jcc.20084.
34. Yang Z, Lasker K, Schneidman-Duhovny D, Webb B, Huang CC, Pettersen EF, Goddard TD, Meng EC, Sali A, Ferrin TE. (2012) UCSF Chimera, Modeller, and IMP: An Integrated Modeling System. J. Struct. Biol. 179:269–279, doi:10.1016/j.jsb.2011.09.006.
35. Šali A, Blundell TL. (1993) Comparative Protein Modelling by Satisfaction of Spatial Restraints. J. Mol. Biol. 234:779–815, doi:10.1006/jmbi.1993.1626.
36. Hanwell MD, Curtis DE, Lonie DC, Vandermeersch T, Zurek E. (2012) Hutchison, G.R. Avogadro: An Advanced Semantic Chemical Editor, Visualization, and Analysis Platform. J. Cheminform. 4, 1–17, doi:10.1186/1758-2946-4-17.
37. Hagberg AA, Schult DA, Swart PJ. (2008) Exploring Network Structure, Dynamics, and Function Using NetworkX. In Proceedings of the Proceedings of the 7th Python in Science Conference (SciPy 2008); Varoquaux, G., Vaught, T., Millman, J., Eds.; Pasadena, CA USA, pp. 11–15.
38. Valdés-Tresanco MS, Valdés-Tresanco ME, Valiente PA, Moreno E. (2021) Gmx_MMPBSA: A New Tool to Perform End-State Free Energy Calculations with GROMACS. J. Chem. Theory Comput. 17:6281–6291, doi:https://doi.org/10.1021/acs.jctc.1c00645.
39. Miller BR, McGee TDJ, Swails JM, Homeyer N, Gohlke H. (2012) Roitberg, A.E. MMPBSA.Py: An Efficient Program for End-State Free Energy Calculations. J. Chem. Theory Comput. 8, 3314–3321, doi:10.1021/ct300418h.
40. Makarov IS, Brocklehurst CE, Karaghiosoff K, Koch G, Knochel P. (2017) Synthesis of Bicyclo[1.1.1]Pentane Bioisosteres of Internal Alkynes and Para-Disubstituted Benzenes from [1.1.1]Propellane. Angew. Chemie - Int. Ed. 56, 12774–12777, doi:10.1002/anie.201706799.
41. GROMACS development team Gmx Rms Available online: https://manual.gromacs.org/2023.2/onlinehelp/gmx-rms.html#gmx-rms (accessed on 9 May 2024).
42. Reva BA, Finkelstein AV, Skolnick J. (1998) What Is the Probability of a Chance Prediction of a Protein Structure with an Rmsd of 6 Å? Fold. Des. 3:141–147, doi:10.1016/S1359-0278(98)00019-4.
43. Kurniawan J, Ishida T. (2022)Protein Model Quality Estimation Using Molecular Dynamics Simulation. ACS Omega 7:24274–24281, doi:10.1021/acsomega.2c01475.
44. Tsai H (Gavin), Tsai C, Ma B, Nussinov R. (2004) In Silico Protein Design by Combinatorial Assembly of Protein Building Blocks. Protein Sci. 13, 2753–2765, doi:10.1110/ps.04774004.
45. Knapp B, Frantal S, Cibena M, Schreiner W, Bauer P. (2011) Is an Intuitive Convergence Definition of Molecular Dynamics Simulations Solely Based on the Root Mean Square Deviation Possible? J. Comput. Biol. 18, 997–1005, doi:10.1089/cmb.2010.0237.
46. Carugo O, Pongor S. (2001) A Normalized Root-mean-spuare Distance for Comparing Protein Three-dimensional Structures. Protein Sci. 10, 1470–1473, doi:10.1110/ps.690101.
47. Maruyama Y, Igarashi R, Ushiku Y, Mitsutake A. (2023) Analysis of Protein Folding Simulation with Moving Root Mean Square Deviation. J. Chem. Inf. Model. 63:1529–1541, doi:10.1021/acs.jcim.2c01444.
48. Paul F, Meng Y, Roux B. (2020) Identification of Druggable Kinase Target Conformations Using Markov Model Metastable States Analysis of Apo-Abl. J. Chem. Theory Comput. 16:1896–1912, doi:10.1021/acs.jctc.9b01158.
49. Paul F, Thomas T, Roux B. (2020) Diversity of Long-Lived Intermediates along the Binding Pathway of Imatinib to Abl Kinase Revealed by MD Simulations. J. Chem. Theory Comput. 16:7852–7865, doi:10.1021/acs.jctc.0c00739.
50. Meng Y, Gao C, Clawson DK, Atwell S, Russell M, Vieth M, Roux B. (2018) Predicting the Conformational Variability of Abl Tyrosine Kinase Using Molecular Dynamics Simulations and Markov State Models. J. Chem. Theory Comput. 14:2721–2732, doi:10.1021/acs.jctc.7b01170.
51. Castro-Alvarez A, Costa AM, Vilarrasa J. (2017) The Performance of Several Docking Programs at Reproducing Protein-Macrolide-like Crystal Structures. Molecules 22, doi:10.3390/molecules22010136.
52. Ramírez D, Caballero J. (2018) Is It Reliable to Take the Molecular Docking Top Scoring Position as the Best Solution without Considering Available Structural Data? Molecules 23:1–17, doi:10.3390/molecules23051038.
53. Hantschel O, Grebien F, Superti-Furga G. (2012) The Growing Arsenal of ATP-Competitive and Allosteric Inhibitors of BCR-ABL. Cancer Res. 72:4890–4895, doi:10.1158/0008-5472.CAN-12-1276.
54. Lu X, Zhang Z, Ren X, Wang D, Ding K. (2017) Synthesis and Identification of GZD856 as an Orally Bioavailable Bcr-AblT315I Inhibitor Overcoming Acquired Imatinib Resistance. J. Enzyme Inhib. Med. Chem. 32:331–336, doi:10.1080/14756366.2016.1250757.
55. Sapir L, Harries D. (2017) Revisiting Hydrogen Bond Thermodynamics in Molecular Simulations. J. Chem. Theory Comput. 13:2851–2857, doi:10.1021/acs.jctc.7b00238.
56. Genheden S, Ryde U. (2015) The MM/PBSA and MM/GBSA Methods to Estimate Ligand-Binding Affinities. Expert Opin. Drug Discov. 10:449–461, doi:10.1517/17460441.2015.1032936.
57. Wang E, Sun H, Wang J, Wang Z, Liu H, Zhang JZH, Hou T. (2019) End-Point Binding Free Energy Calculation with MM/PBSA and MM/GBSA: Strategies and Applications in Drug Design. Chem. Rev. 119:9478–9508, doi:10.1021/acs.chemrev.9b00055.
58. Daina A, Zoete V. (2016) A BOILED-Egg To Predict Gastrointestinal Absorption and Brain Penetration of Small Molecules. ChemMedChem 11:1117–1121, doi:10.1002/cmdc.201600182.
59. Zhu Y, Zhu Y, Miao L, Jia T, Mao J, Xue L, Wang Y. (2023) Comparison of the Efficacy and Safety of Ponatinib and Dasatinib in Philadelphia Chromosome-Positive Acute Lymphoblastic Leukemia With Central Nervous System Relapse: A Retrospective Study. Technol. Cancer Res. Treat. 22, doi:10.1177/15330338231165866.
60. Ravi K, Franson A, Homan MJ, Roberts H, Pai MP, Miklja Z, He M, Wen B, Benitez LL, Perissinotti AJ, *et al.* (2021) Comparative Pharmacokinetic Analysis of the Blood-Brain Barrier Penetration of Dasatinib and Ponatinib in Mice. Leuk. Lymphoma 62:1990–1994, doi:10.1080/10428194.2021.1894647.
61. Ahrari S, Mogharrab N, Navapour L. (2017) Interconversion of Inactive to Active Conformation of MARK2: Insights from Molecular Modeling and Molecular Dynamics Simulation. Arch. Biochem. Biophys. 630, 66–80, doi:10.1016/j.abb.2017.07.002.